



Project FORTE - Nuclear Thermal Hydraulics Research & Development

Application of CFD to single-phase Natural Convection Loops for Nuclear Passive Safety Systems

August 2019



FNC 53798/48655R Issue 1
SYSTEMS AND ENGINEERING TECHNOLOGY

An introduction to Project FORTE

The Department for Business, Energy and Industrial Strategy (BEIS) has tasked Frazer-Nash Consultancy and its partner organisations to deliver the first phase of a programme of nuclear thermal hydraulics research and development.

Phase 1 of the programme comprises two parts:

- ▶ The specification and development of innovative thermal hydraulic modelling methods and tools; and
- ▶ The specification of a new United Kingdom thermal hydraulics test facility.

The work is intended to consider all future reactor technologies including Gen III+, small modular reactors and advanced reactor technologies.

Our project partners

The team is led by Frazer-Nash Consultancy and includes:



The
University
Of
Sheffield.



Westinghouse



The University of Manchester



**Science & Technology
Facilities Council**

For more information, visit www.innovationfornuclear.co.uk/nuclearthermalhydraulics.html

Executive Summary

This report describes research that has been undertaken to provide insight into the thermal hydraulic phenomena associated with Natural Circulation Loops (NCL) through numerical simulation with state-of-the-art RANS CFD models.

Natural Circulation Loops offer potential for use as part of the passive safety systems being developed both for current Generation III and III+, and future Generation IV, reactor concepts. By exploiting natural convection phenomena, Natural Circulation Loops allow thermal energy to be transported away from the reactor core and exchanged with an external thermal sink, without the need for mechanical pumps or operator intervention. Designed and implemented correctly, this feature of NCLs can allow for essential reactor cooling to continue during a station blackout or other severe accident scenario.

Key to the design of such systems is the ability to predict their performance. CFD simulations have the potential to provide detailed solutions to the kinds of complex nuclear thermal hydraulic problems posed by NCLs. The additional insight offered by these solutions should also help further develop our understanding of the thermal hydraulic phenomena involved; something which will be crucial if passive cooling systems are to be utilized effectively.

This research involved the solution of a series of simplified two-dimensional natural circulation loops of different aspect ratios over a wide range of Rayleigh numbers ($8 \times 10^9 < Ra_m < 8 \times 10^{15}$). The loops feature a horizontally oriented heater, which provides a fixed heat flux, and a vertically oriented cooler, the surface of which is maintained at a fixed temperature. The Unsteady Reynolds-averaged Navier-Stokes (URANS) framework has been applied with a linear $k-\varepsilon$ eddy-viscosity turbulence model and a low- Re near-wall approach. The purpose of the work is to study the transient evolution of the flow as it moves from rest to a 'steady-state' flow condition.

Results predict that the NCL system exhibits complex dynamic behaviour, with strong sensitivity to the imposed Rayleigh number. Initial thermal transients led to the establishment of unstable and oscillatory flow behaviour which, in most cases, resulted in complete flow reversals.

Overall, a number of key conclusions can be drawn from this work:

- ▶ A two-dimensional loop model, with a linear eddy-viscosity turbulence model, is able to broadly reproduce the correct statistical system response as Ra_m is increased.
- ▶ The Unsteady Reynolds-averaged Navier-Stokes turbulence modelling framework is capable of reproducing complex transient buoyant features which are, at least with the model considered in this work, integral to the dynamic evolution of the flow within the loop.
- ▶ Order-of-magnitude increases in Ra_m are seen to significantly alter the predicted dynamic response of the system. With further validation, this has implications for real systems whose power inputs might additionally vary with time.
- ▶ There is a clear need for high fidelity, openly available, experimental and numerical datasets for NCL, and other, flows relevant to nuclear thermal hydraulics. This would enable further assessment and testing of the CFD approach to be conducted.

Whilst the two-dimensional model allows solutions to be obtained relatively quickly, and has allowed a number of different input parameters and geometries to be assessed in this work, recommendations have been made to extend and develop this research further.

Contents

1	INTRODUCTION	5
2	NATURAL CIRCULATION LOOP ANALYSIS	7
3	NUMERICAL MODELLING	10
3.1	Mesh	12
3.2	Equations	15
3.3	Time step	17
3.4	CFD Model Solver	17
4	RESULTS	18
4.1	Mesh sensitivity	18
4.2	Description of predicted start-up flow behaviour	19
4.3	Statistically steady-state behaviour	23
4.4	Predicted effect of increasing Rayleigh number	25
4.5	Comparisons with existing correlations	28
5	CONCLUSIONS	30
6	REFERENCES	32

1 Introduction

The use of passive safety systems in nuclear power has been discussed since at least the mid 1980's, where it was recognized that they have the potential to contribute towards the simplification, safety and improved economics of new Nuclear Power Plant (NPP) designs (IAEA 2005). As a result, these types of systems are being considered for numerous current reactor concepts, including Generation III and III+ light water reactors (LWR), and are also expected to play a significant role in the development of future Generation IV reactors (Gen IV International Forum 2013).

A number of passive safety systems are based on the concept of a *Natural Circulation Loop* (NCL). This is a closed circuit where fluid flow is driven solely by the density differences arising from thermal imbalance. By arranging such a system so that it contains mechanisms to both impart and extract thermal energy from the fluid, it becomes possible to intentionally transport heat from a high-temperature source (i.e. the reactor core) to a low temperature sink without recourse to pumps or other mechanical devices. Implemented correctly, NCLs can potentially allow for essential reactor cooling to continue during a station blackout or other severe accident scenario, without the need for any source of external power or operator intervention.

The Passive Residual Heat Removal (PRHR) system incorporated into the Westinghouse AP1000 reactor design¹ (Schulz 2006) is one example of a NCL based passive safety system. The PRHR consists of a C-Tube type heat exchanger immersed within the In-containment Refuelling Water Storage Tank (IRWST) which is located above the main reactor and coolant loops. As shown in Figure 1, an inlet line attached to one of the hot legs of the main coolant loop feeds the C-Tube heat exchanger which, after exchanging core decay heat into the IRWST, then returns to join the cold leg of the reactor coolant system to recirculate through the core. The circulation within this loop is solely driven by the fluid density differences arising from temperature difference between the reactor core and the IRWST.

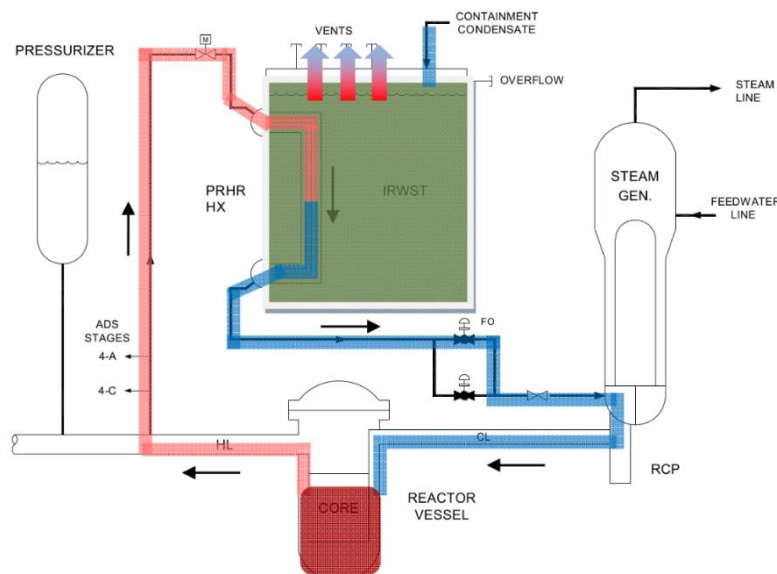


Figure 1: Schematic of the Passive Residual Heat Removal System (PHRS) incorporated into the Westinghouse AP1000 nuclear reactor

¹ The Westinghouse AP1000 is a Generation III+ PWR reactor design which has received design certification by both the US based Nuclear Regulatory Commission (2005) and, more recently, the UK's Office for Nuclear Regulation (2017).

The IRWST has the capacity to absorb decay heat for around an hour before it will begin to boil but, once boiling, the steam rises to the roof of the steel containment vessel where it is cooled, condensed by a secondary passive safety system (which also relies on natural convection, called the Passive Containment Cooling System), and then ultimately returned to the IRWST. Together, both of these systems can provide indefinite decay heat removal capability with no operator action required (Schulz 2006).

Whilst some next-generation nuclear reactors, like the AP1000, are clearly already realising the potential of using NCLs for enhanced nuclear safety, a challenge remains in the effective design and substantiation of these systems. A review of the application of NCL systems in nuclear thermal hydraulics by Basu *et al.* (2014) found that the use of multidimensional numerical tools in the nuclear community has only recently become a topic of interest. The numerical modelling methodology currently favoured by the nuclear industry makes use of “system codes”.

These “system codes” are often 1D and generally rely heavily on empirical and scale-dependent correlations obtained via experimentation. Whilst these have been shown to provide reliable predictions of integral parameters (though limited, of course, to the parameter ranges that the underlying correlations were developed for), these code cannot reproduce the significant complex local effects inherent to natural convection phenomena which can influence the overall system behaviour. Ultimately, this lack of fidelity translates into large uncertainties, large safety margins and increased costs (IAEA 2009).

Modern general purpose multidimensional Computational Fluid Dynamics (CFD) codes, used extensively in other fields, have now reached a degree of maturity for the prediction of single-phase buoyant flows, see, for example, Ammour *et al.* (2013) and Omranian *et al.* (2014)). Therefore, if properly verified and validated, they have the potential to provide detailed, reliable and accurate solutions to the kinds of complex nuclear thermal hydraulic problems posed by NCLs and other related systems. The additional insight offered by these solutions should also help further develop our understanding of the thermal hydraulic phenomena involved; something which will be crucial if passive cooling systems are to be designed and utilized effectively (IAEA 2009).

This work aims to provide further insight into the prediction of the complex transient behaviour of NCLs through a series of unsteady 2D numerical simulations at a range of Rayleigh numbers, and for different loop geometries. Solving in 2D allows simulations to be performed relatively quickly, and without significant computation expense, whilst still capturing a significant proportion of the predicted flow physics.

Aside from being interesting in their own right, they will also help to identify cases that might be suitable for further study using higher fidelity 3D techniques, including Large Eddy Simulation or Direct Numerical Simulation, which can provide valuable validation data for simpler methods. The simulations also aim to further demonstrate the potential of the Unsteady Reynolds-Averaged Navier-Stokes (URANS) framework in resolving the complex transient flows and natural convection phenomena associated with nuclear thermal hydraulics.

It should be noted that these studies are academic in nature and are not intending to represent any particular reactor design or system. They are aimed at improving understanding of both the way in which the detailed, small scale flow phenomena may affect the bulk flow and the potential of CFD techniques to make a contribution to future reactor design in this area.

2 Natural Circulation Loop Analysis

At their most basic, a NCL consists of a closed circuit with a thermal energy source positioned below a thermal energy sink. A number of possible configurations exist, differing mainly in the arrangement or orientation of the thermal source and sink. A schematic of a generic NCL can be seen in Figure 2, where a cooler is positioned along the top leg and a heater along the bottom leg.

Clearly different arrangements will affect both the thermal hydraulic performance and the stability of the system. The horizontal heater, horizontal cooler arrangement considered in Figure 2 will be, a priori, unstable due to the resulting buoyancy force lacking a preferential direction. Conversely, a system in which both the heater and cooler are vertically oriented would be expected to be more stable.

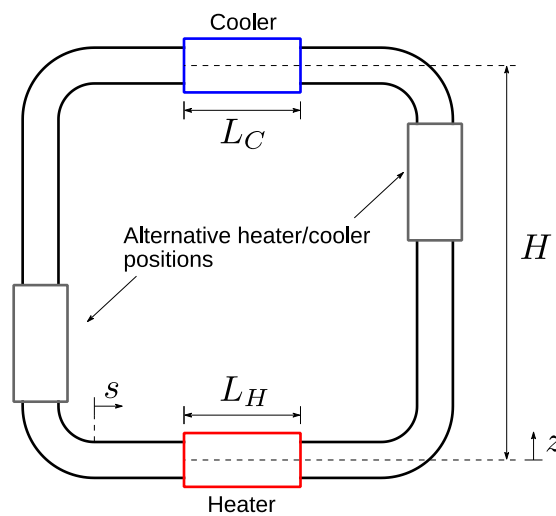


Figure 2: Simple Natural Circulation Loop

By conducting a one-dimensional analysis of a simple loop system, such as the one considered above, Vijayan (2002) determined the 1D momentum equation governing motion of fluid around a uniform diameter loop is:

$$\frac{L_t}{A} \frac{d\dot{m}}{dt} = -g \oint \rho dz - \frac{\dot{m}^2}{2\rho_0 A^2} \left(\frac{fL_t}{D_h} + K \right) \quad 1$$

where L_t is the total length along the centreline of the loop, \dot{m} is the mass flow rate, f is the friction factor, D_h is the hydraulic diameter [m], ρ_0 is a reference density [kg m^{-3}] and K is a loss coefficient that accounts for pressure losses due to bends. In obtaining Equation 1, the fluid is assumed to be incompressible and the Boussinesq approximation for buoyancy is used².

The net buoyancy term, the first term on the RHS of Equation 1, results from the difference between the average density of the left side and right side, multiplied by the height over which that density variation occurs. A steady state will result if the driving buoyancy force is balanced by the retarding friction force. The temperature rise across the heater is given by

² The Boussinesq approximation is considered further in Section 3.2.1, but states that fluid properties can be considered constant in the governing equations except for the density in the buoyancy force term, which is assumed to vary linearly with temperature.

$$\Delta T_h = \frac{Q_h}{\dot{m}c_p} \quad 2$$

where Q_h is the total heat input rate into the heater [W] and c_p is the specific heat capacity [$\text{Jkg}^{-1}\text{K}^{-1}$]. If a steady state is reached, then we expect the heat lost through the cooler to equal the heat input rate to the heater.

Owing to these unique properties of NCLs, there has been a significant amount of interest in their stability and steady state behaviour; see, for example, Vijayan & Austregesilo (1994), Vijayan (2002) and Vijayan *et al.* (1991). By non-dimensionalising Equation 1 using a suitable choice of scales, and additionally considering the 1D energy equation governing the system, Vijayan (2002) determined that the system can be specified through a modified version of the Grashof number:

$$Gr_m = \frac{D_h^3 \rho_0^2 \beta g \Delta \theta_r}{\mu^2} \quad 3$$

where D_h is the hydraulic diameter of the pipe [m], ρ_0 is a reference density [kg m^{-3}], β is the fluid volume expansion coefficient [K^{-1}], g is acceleration due to gravity [m s^{-2}] and μ is the fluid viscosity [$\text{kg m}^{-1} \text{s}^{-1}$]. The reference temperature difference, $\Delta \theta_r$, is defined as:

$$\Delta \theta_r = \frac{Q_h \Delta Z}{A \mu c_p} \quad 4$$

where ΔZ is the vertical elevation between the centre of the heater and the cooler [m], and A is the cross-sectional area of the pipe [m^2]. Since $Ra = Gr \cdot Pr$, we can then define a modified Raleigh number as:

$$Ra_m = \frac{D_h^3 \rho \beta g Q_h \Delta Z}{\alpha \mu^2 A c_p} \quad 5$$

where α is the thermal diffusivity of the fluid [$\text{m}^2 \text{s}^{-1}$].

By assuming that a steady state exists, and by utilizing friction factors for laminar and turbulent flow (the latter assumes Blasius correlations to be valid), Vijayan (2002) relates the modified Grashof number (as the primary input) to the steady state Reynolds number of the flow around the loop that results (i.e. the output):

$$Re_{ss} = C \left(\frac{Gr_m}{N_G} \right)^r \quad 6$$

The steady state Reynolds number, Re_{ss} , can be defined in terms of the steady state mass flow rate, \dot{m}_{ss} :

$$Re_{ss} = \frac{D_h \dot{m}_{ss}}{A \mu} \quad 7$$

N_G is a geometric parameter which non-dimensionalizes the length of the loop, L_t :

$$N_G = \frac{L_t}{D_h} \quad 8$$

Values of the constants C and r in Equation 6, as proposed by (Vijayan 2002), are shown in Table 1.

Flow Condition	c	r
Laminar	0.1768	0.5
Turbulent	1.96	1/2.75

Table 1: Constants for the correlation in Equation 6

Vijayan (2002) collated results for the non-dimensional parameters in Equation 6 from a wide selection of experiments. These are plotted, together with the correlations, in Figure 3 where it can be seen that the correlations provide good agreement with the various sets of experimental data surveyed. Unfortunately, the experiments covered by Figure 3 do not provide any detailed flow measurements that would invite numerical reproduction.

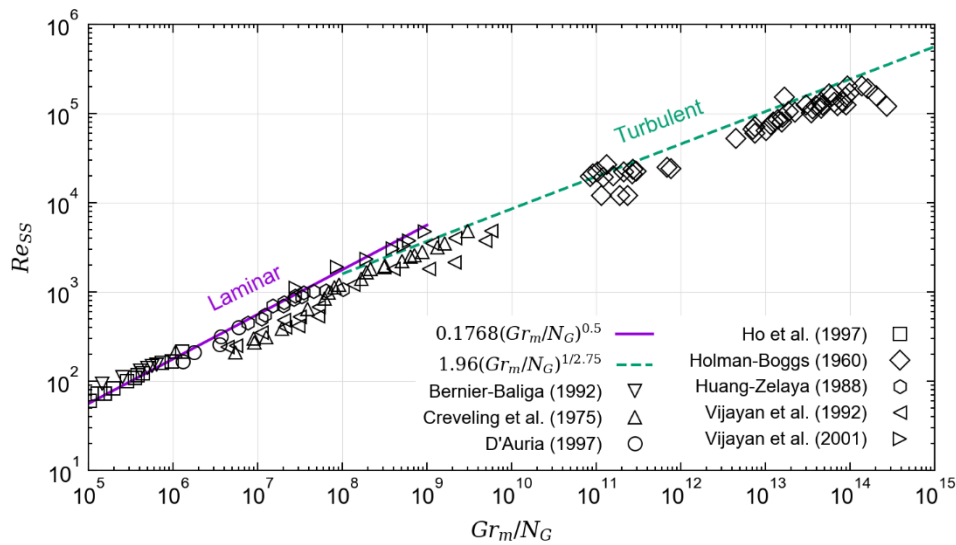


Figure 3: Steady state natural circulation flow in uniform diameter loops, plotting the modified Grashof number Gr_m/N_G against the resultant steady state Reynolds number Re_{ss} for a number of experimental data sets. The correlations suggested by Vijayan (2002) have also been plotted

There are a limited number of CFD studies on NCLs available in the open literature. Wang *et al.* (2013) presented 3D numerical results for a square loop with a cooler on the upper horizontal leg and a heater on the lower horizontal leg. Comparisons of global parameters (Re , Gr) with prior experiments by Misale *et al.* (2007) demonstrated good agreement, but some discrepancies were noted when comparing the time-history of the temperature difference across the heater.

A recent numerical study by Kudariyawar *et al.* (2016) provided 3D steady state and transient CFD simulations for NCLs with various configurations of heaters and coolers. Results showed good agreement with the experimental correlations of Vijayan *et al.* (1991) and demonstrated interesting transient behaviour but, as with the study by Wang *et al.* (2013), a lack of high fidelity experimental or numerical data prevented complete validation of the three-dimensional flow and thermal fields.

3 Numerical modelling

Since a comprehensive survey of the open literature revealed no ‘CFD grade’ experimental data that would be suitable for reproduction and validation, numerical simulations were conducted on a geometrically simple loop, similar to that seen in Figure 2. The loop is designed to be simple enough to enable efficient computation with URANS (or, at some point in the future, LES) methods but relevant enough to provide both insight into NCL thermal hydraulic performance and a preliminary assessment of the capability of CFD methods in reproducing such flows.

The specific case under consideration comprises a two-dimensional³ loop with a horizontal oriented heater, which provides a fixed heat flux, and a vertical oriented cooler, the surface of which is maintained at a fixed temperature. Two loop geometries are considered, as shown in Figure 4, which differ only in their aspect ratio. Non-dimensional relationships between the various geometric parameters are detailed in Table 2; note that the absolute value of the parameters is unimportant providing the non-dimensional relationships are preserved.

Following the non-dimensional analysis proposed by (Vijayan 2002), the flow conditions are specified in a completely non-dimensional fashion using a Rayleigh number based on a modified Grashof number, $Ra_m = Gr_m \cdot Pr$, as per Equation 5. Material properties appearing in Equation 5 are chosen arbitrarily; so long as they combine to give the correct non-dimensional parameters there is no loss of generality. Four different Rayleigh numbers are considered $Ra_m = 10^9, 10^{11}, 10^{13}$ and 10^{15} , with only the first three of these applied to the tall loop. A Prandtl number of $Pr = 7.1$ is used. These cases were selected to provide reasonable coverage of the parameter range covered by the correlations presented in Figure 3. Table 3 provides a list of all cases computed as part of the current work.

All simulations began from stagnant conditions to enable the initial transient evolution of the flow to be captured. Using the correlations provided by Vijayan, it is possible to predict the steady state Reynolds number that should result from a given Ra_m (if such a steady state is reached). From the definition of the Reynolds number (Equation 7) and the specified fluid properties, a value of the steady state mass flow rate, \dot{m}_{ss} , is obtained. Equation 2 can then be used to compute the predicted temperature rise across the heater, $(\Delta T_h)_{ss}$, if the flow does reach a steady state.

These two values have been used to non-dimensionalise the results presented later in Section 4. In addition, the initial bulk temperature of the fluid, T_i , was specified as

$$T_i = T_c + 2(\Delta T_h)_{ss} \quad 9$$

where T_c is the fixed temperature assigned to the cooler walls. Since this implies an initial temperature relatively close to the cooler wall temperature, the (fixed) heat flux imposed by the heater is expected to be initially dominant. The bulk temperature in the loop will be expected to rise in time, until the heat flux exiting the cooler (which has a fixed temperature) has increased to match the imposed heater heat flux. After this, statistical thermal equilibrium will be observed. The cooler temperature is the only fixed temperature within the system. For the remainder of the loop, adiabatic and no-slip conditions are set.

Preliminary computations with an initial temperature much higher than the cooler wall temperature showed that, whilst the cooler heat flux did initiate motion in the loop, hot fluid would tend to collect in the upper horizontal leg (i.e. cause stratification in the loop). This ‘hot plug’ was seen to severely restrict, though not eliminate, fluid motion through the affected leg

³ Note that this is not solved as axi-symmetric. Thus, the 2D slice strictly represents a cross-section of an infinitely wide duct rather than a pipe.

and this, in turn, significantly increased the time required for the cooler to reduce the bulk temperature in the loop (and thus eliminate the stratification). The additional computational time implied by this unfortunately prohibited further computation of the case.

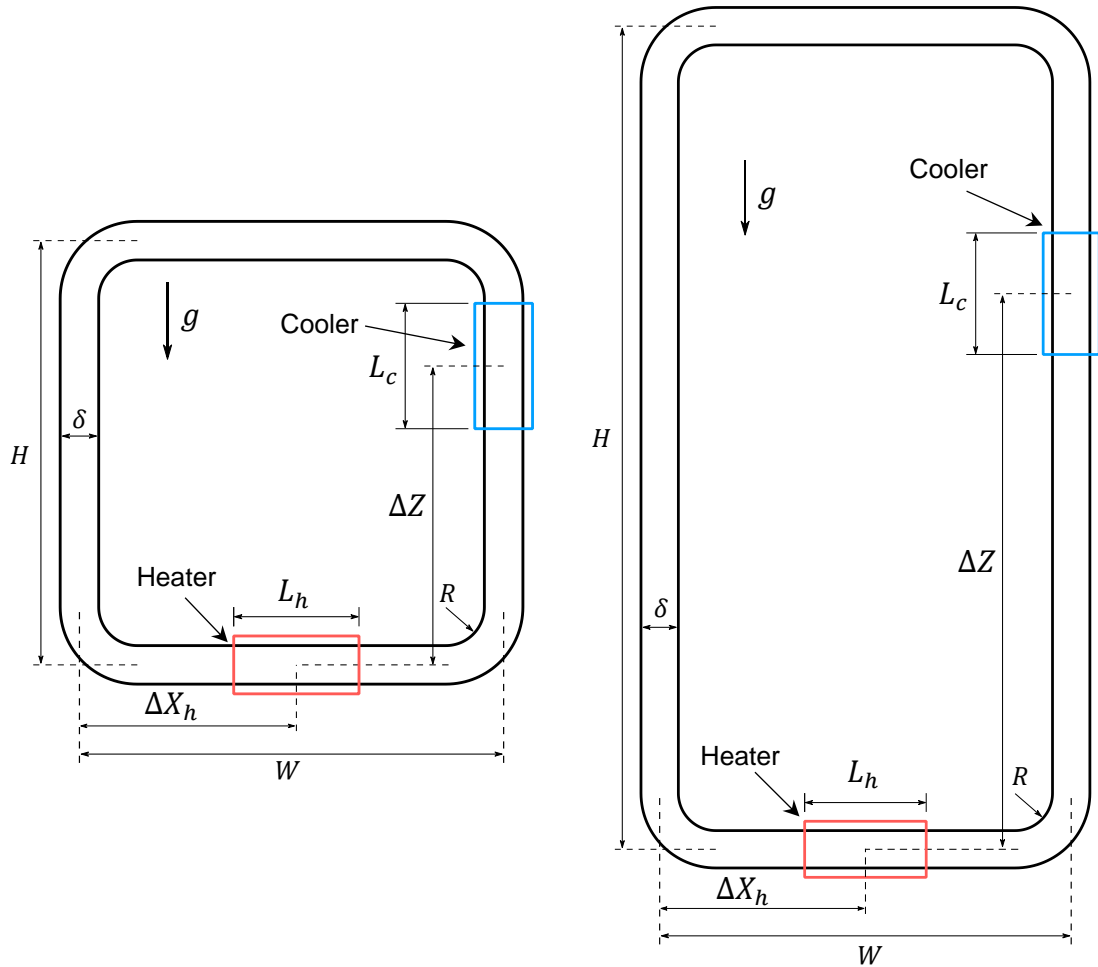


Figure 4: Geometry for square (left) and tall (right) loops. The red and blue boxes only indicate the positions of the heater and cooler; thermal boundary conditions are applied directly to the channel walls. δ is the height of the channel.

Element	Relation	Square loop	Tall loop
H	$\frac{H}{\delta}$	10	20
W	$\frac{H}{W}$	1	2
R	$\frac{R}{\delta}$	1.5	1.5
ΔZ	$\frac{\Delta Z}{H}$	0.675	0.675
ΔX_h	$\frac{\Delta X_h}{W}$	0.5	0.5
L_h, L_c	$\frac{L_i}{\delta}$	3.5	3.5

Table 2: Non-dimensional geometric relations for the NCLs considered in Figure 4

Case	H/W	Pr	Ra_m	Gr_m	N_G	Gr_m/N_G	Re_{SS}
Square loop							
ncl-ra1e9-s	1	7.1	8×10^9	1.127×10^9	18.7125	6.022×10^7	1.372×10^3
ncl-ra1e11-s	1		8×10^{11}	1.127×10^{11}		6.022×10^9	7.056×10^3
ncl-ra1e13-s	1		8×10^{13}	1.127×10^{13}		6.022×10^{11}	3.765×10^4
ncl-ra1e15-s	1		8×10^{15}	1.127×10^{15}		6.022×10^{13}	3.765×10^5
Tall loop							
ncl-ra1e9-t	2	7.1	8×10^9	1.127×10^9	28.7125	3.924×10^7	1.107×10^3
ncl-ra1e11-t	2		8×10^{11}	1.127×10^{11}		3.924×10^9	6.038×10^3
ncl-ra1e13-t	2		8×10^{13}	1.127×10^{13}		3.924×10^{11}	3.222×10^4

Table 3: Input parameters for cases computed as part of the current work. H/W , Pr and Ra_m are chosen and define the case. The remaining quantities are derived from Equations 3, 6 and 8.

3.1 Mesh

Block structured meshes comprising hexahedral elements are utilized with a low- Re wall modelling approach (i.e. with $y^+ \approx 1$) adopted for all Rayleigh numbers considered. Clearly mesh requirements increase with the Rayleigh number and thus a mesh was created for each combination of Ra and loop geometry considered in Table 3. An initial estimate for the size of the first cell was obtained by assuming a pipe flow at the steady-state Reynolds number computed by the correlation given in Equation 6. First an estimate of the wall shear stress is obtained from

$$\tau_w = \frac{1}{8} f \rho U_{avg}^2 \quad 10$$

U_{avg} is determined from the Reynolds number and the fluid properties that were used to compute Ra_m . The friction factor, f , is then computed using the well-known Blasius correlation⁴

⁴ Note that this correlation was also used by Vijayan (2002) in arriving at the correlation in Equation 6.

$$f = \frac{p}{Re^b} \quad 11$$

where $p = 64$, $b = 1$ for laminar flow and $p = 0.316$, $b = 0.25$ for turbulent flow. Finally, the distance to the first node can then be estimated through

$$y = \frac{\mu y^+}{\sqrt{\tau_w/\rho}} \quad 12$$

where y^+ is set equal to 1; the value desired. Whilst the transient and unstable nature of the expected flow may result in flow rates which locally exceed Re_{SS} , and thus render $y^+ > 1$ for the first node, y^+ would be expected to remain at least of the same order during the entire calculation. Wall-parallel node resolutions were chosen to ensure cell aspect ratios of $\mathcal{O}(1)$ in the loop centre.

Details of the resultant meshes used in all computations are presented in Table 4 and those for the square loop are illustrated in Figure 5. All of the meshes were produced using the meshing package ANSYS ICEMCFD v19.2.

The sensitivity of the solution to the mesh sizing was also investigated for the square case at $Ra_m = 8 \times 10^{13}$. Two additional meshes were produced which increased node resolution consecutively while keeping the distance to the first wall-normal node constant. Details of these meshes are presented in Table 5 and illustrations are provided in Figure 6.

Case	Ra_m	Total Nodes, N	N_{\perp}	N_{\parallel}	Δy
Square loop					
ncl-ra1e9-s	8×10^9	41,600	65	640	0.005δ
ncl-ra1e11-s	8×10^{11}	44,800	70	640	0.001δ
ncl-ra1e13-s*	8×10^{13}	89,600	70	1280	0.001δ
ncl-ra1e15-s	8×10^{15}	115,200	90	1280	0.0001δ
Tall loop					
ncl-ra1e9-t	8×10^9	49,000	50	980	0.005δ
ncl-ra1e11-t	8×10^{11}	68,600	70	980	0.001δ
ncl-ra1e13-t	8×10^{13}	137,760	70	1968	0.001δ

Table 4: Mesh parameters used for each case considered. N_{\perp} and N_{\parallel} represents the node count in the wall-normal and wall-parallel directions respectively. Δy is the distance to the first node where δ is the channel height. *This mesh corresponds to mesh “ncl-ra1e13-s-r2” in Table 5.

Mesh	Total Nodes, N	N_{\perp}	N_{\parallel}	Δy
ncl-ra1e13-s-r1	44,800	70	640	0.001δ
ncl-ra1e13-s-r2*	89,600	70	1280	0.001δ
ncl-ra1e13-s-r3	268,800	105	2560	0.001δ

Table 5: Mesh parameters used in sensitivity study. *This mesh corresponds to mesh “ncl-ra1e13-s” in Table 4

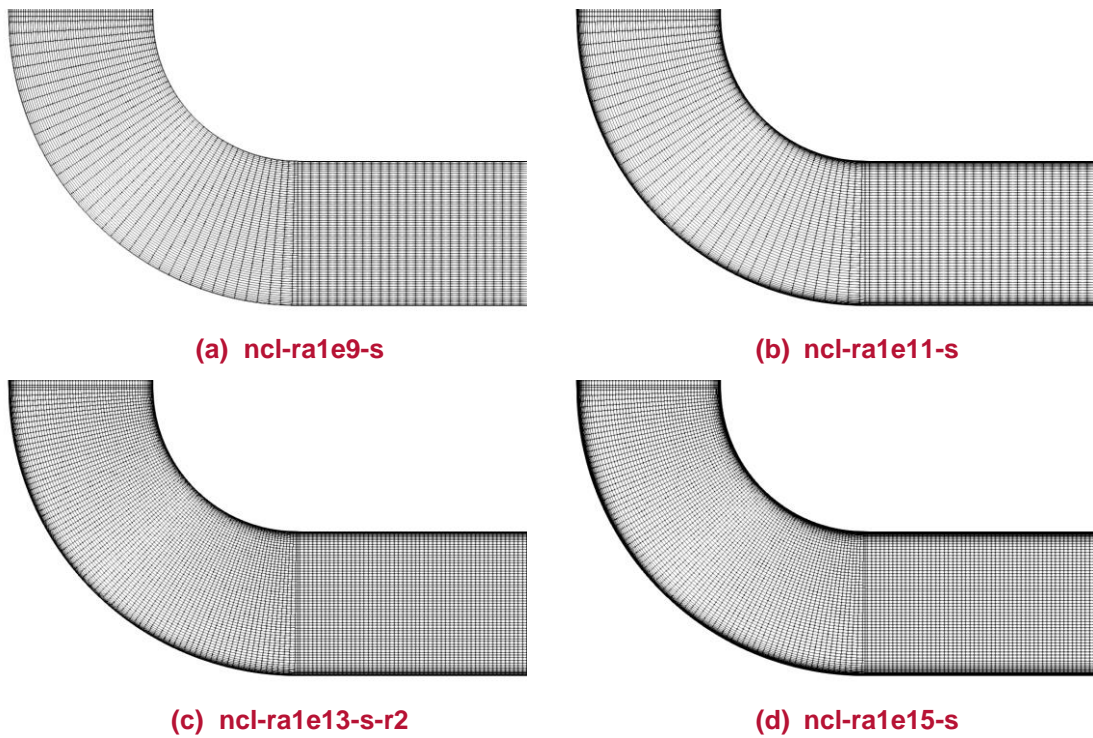


Figure 5: Close up of the bottom left elbow of the low- Re meshes generated for the square loop considered in Figure 4. See Table 4 for mesh details

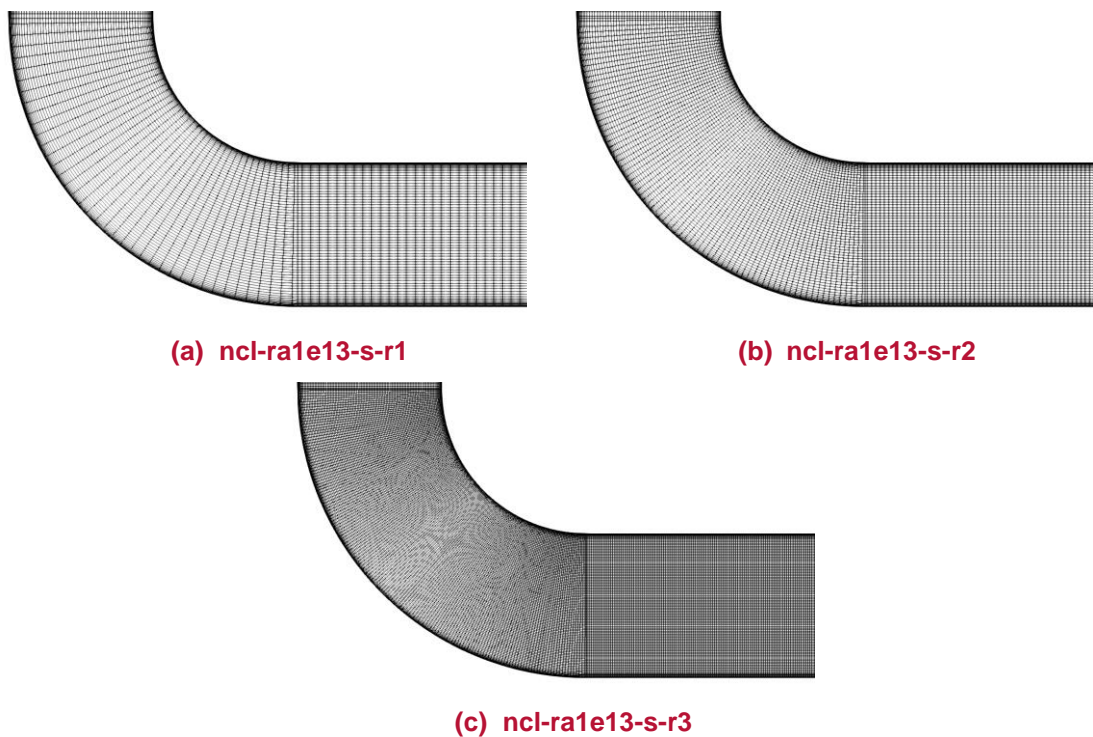


Figure 6: Close up of the bottom left elbow of the low- Re meshes generated for the mesh sensitivity study. See Table 5 for mesh details

3.2 Equations

Transient simulations are performed under the Unsteady Reynolds-Averaged Navier-Stokes (URANS) framework using ensemble averaged forms of the continuity, momentum and scalar temperature transport equations:

$$\frac{\partial U_i}{\partial x_i} = 0 \quad 13$$

$$\rho \left(\frac{\partial U_i}{\partial t} + U_j \frac{\partial U_i}{\partial x_j} \right) = \frac{\partial P}{\partial x_i} + \frac{\partial}{\partial x_j} \left[\mu \left(\frac{\partial U_i}{\partial x_j} + \frac{\partial U_j}{\partial x_i} \right) - \rho \overline{u_i u_j} \right] + \rho g_i \quad 14$$

$$\frac{\partial T}{\partial t} + U_j \frac{\partial T}{\partial x_j} = \frac{\partial}{\partial x_j} \left[\alpha \frac{\partial T}{\partial x_j} - \overline{u_j \theta} \right] \quad 15$$

where μ , the fluid viscosity, and α , the fluid thermal diffusivity, are constant. Treatment of the fluid density, ρ , and the buoyancy body force ρg_i are discussed in Section 3.2.1 and provision of the Reynolds stresses, $\overline{u_i u_j}$, and turbulent heat flux $\overline{u_j \theta}$ are discussed in Section 3.2.2.

3.2.1 Buoyancy

The effects of buoyancy are incorporated by utilizing the Boussinesq approximation. This states that the density can be considered constant in the governing equations, except when multiplied by acceleration due to gravity in the buoyancy force term. Thus, the density is treated as constant, and equal to the reference density ρ_0 , everywhere in Equation 14 except in the final buoyancy force term, ρg_i . Density variations are then incorporated by assuming a linear dependence with temperature. The buoyancy force term, ρg_i , becomes:

$$\rho g_i = \rho_0 g_i - \rho_0 g_i \beta (T - T_0) \quad 16$$

where ρ_0 and T_0 are the reference density and temperature respectively. The reference temperature T_0 is taken as $1/\beta$ and since the flow is solved in a completely non-dimensional fashion, ρ_0 and β can be chosen arbitrarily so long as they produce the desired Gr_m .

The Boussinesq approximation is widely used to solve internal natural convection flows within the URANS framework and considerably simplifies the analysis by removing the need to solve an equation of state. It is valid so long as relative density variations are not too large (i.e. $\Delta\rho/\rho_0 < 1$); something which is broadly satisfied for the present simulations except close to the upper heater wall in the higher Ra_m cases. The use of the approximation is thus considered reasonable for the simplified 2D flows considered here, but any extension of this work to 3D, or to a specific loop with a specific fluid, should further consider whether the approximation is appropriate.

3.2.2 Turbulence modelling

The Launder-Sharma (1974) low- Re form of the standard k - ε model is used for the turbulence. This is a well-established low- Re two-equation linear eddy-viscosity model, which has seen wide use across a large number of natural convection studies conducted to date (see, for example, Craft *et al.* (2004), Omranian *et al.* (2014), Wilson *et al.* (2015)). It linearly relates the Reynolds stresses to the mean strains through:

$$\overline{u_i u_j} = \frac{2}{3} k \delta_{ij} - \nu_t \left(\frac{\partial U_i}{\partial x_j} + \frac{\partial U_j}{\partial x_i} \right) \quad 17$$

where ν_t , the turbulent viscosity, is given by:

$$v_t = c_\mu f_\mu \frac{k^2}{\varepsilon} \quad 18$$

where c_μ is a constant and f_μ is a near-wall damping term specified in Table 6.

The turbulent kinetic energy, k , and the dissipation rate, ε , are obtained via modelled transport equations:

$$\frac{\partial k}{\partial t} + U_i \frac{\partial k}{\partial x_i} = \frac{\partial}{\partial x_i} \left[\left(\nu + \frac{\nu_t}{\sigma_k} \right) \frac{\partial k}{\partial x_i} \right] - \overline{u_i u_j} \frac{\partial U_i}{\partial x_j} - \varepsilon - D + F_b \quad 19$$

$$\frac{\partial \tilde{\varepsilon}}{\partial t} + U_i \frac{\partial \tilde{\varepsilon}}{\partial x_i} = \frac{\partial}{\partial x_i} \left[\left(\nu + \frac{\nu_t}{\sigma_\varepsilon} \right) \frac{\partial \tilde{\varepsilon}}{\partial x_i} \right] + (C_{\varepsilon 1} f_{\varepsilon 1} (P_k + F_b) - C_{\varepsilon 2} f_{\varepsilon 2} \tilde{\varepsilon}) \frac{\tilde{\varepsilon}}{k} + S_\varepsilon \quad 20$$

where the terms $f_{\varepsilon 1}$, $f_{\varepsilon 2}$, D and S_ε represent the near-wall damping modifications specified in Table 6. $\tilde{\varepsilon}$ is the so-called quasi-homogenous dissipation rate of k defined as:

$$\tilde{\varepsilon} = \varepsilon - 2\nu \left(\frac{\partial \sqrt{k}}{\partial x_n} \right) \quad 21$$

The buoyant contribution to the turbulent kinetic energy equation, F_b , is given by:

$$F_b = -\beta g_i \overline{u_i \theta} \quad 22$$

where, $\overline{u_i \theta}$, the turbulent heat flux is provided by the simple gradient diffusion hypothesis:

$$\overline{u_i \theta} = -\frac{\nu_t}{\sigma_\alpha} \frac{\partial T}{\partial x_i} \quad 23$$

where σ_α , the turbulent Prandtl number, is taken as 0.9. All model coefficients for the above equations are presented in Table 7.

f_μ	D	$f_{\varepsilon 1}$	$f_{\varepsilon 2}$	S_ε
$\exp \left[\frac{-3.4}{(1 + Re_t/50)^2} \right]$	$2\nu \left(\frac{\partial \sqrt{k}}{\partial x_i} \right)^2$	1	$1 - 0.22e^{-(Re_t/6)^2}$	$2\nu\nu_t \left(\frac{\partial^2 U_i}{\partial x_j \partial x_k} \right)^2$

Table 6: Viscous damping terms and functions for the low- Re k - ε model of Launder-Sharma (1974). The turbulent Reynolds number $Re_t = k^2/\nu\tilde{\varepsilon}$.

C_μ	$C_{\varepsilon 1}$	$C_{\varepsilon 2}$	σ_k	σ_ε
0.09	1.44	1.92	1.0	1.3

Table 7: Model coefficients for the low- Re k - ε model of Launder and Sharma (1974)

For the 2D flows considered in this work, the Launder-Sharma k - ε should provide adequate representation of both the shear driven turbulence and the direct generation of turbulent kinetic energy which results from the fluctuating part of the buoyancy force. In the full 3D geometry, however, the loop bends and localized buoyancy effects (i.e. 3D plume structures and local recirculation regions) present will most likely induce secondary flows. Even though the magnitude of secondary flows is typically only a few percent of the primary flow (which, in this case of an NCL is the pipe flow around the loop) they typically manifest as an addition mixing mechanism within the pipe cross-section. This can lead to noticeable differences in both the mean (primary) velocity profile and the distribution of scalars within the pipe, including temperature.

The level of modelling approach required to adequately capture such secondary flows is considered in more detail in Wilson (2019) but, as these features fundamentally involve flow

curvature, turbulence models based on the linear eddy-viscosity concept (the Launder-Sharma $k-\varepsilon$ used here being no exception) will not be able to fully reproduce them. This is, however, of less importance in the two-dimensional cases considered here, since the possibility of cross-sectional flow structures is excluded. An exploration of more advanced modelling approaches, including those based on full stress-transport, is recommended in any further extension of this work to three-dimensions.

3.3 Time step

To provide a suitable value for the time step, a reference time-scale is constructed by considering the loop circulation time

$$t_r = \frac{V_t \rho_0}{\dot{m}_{ss}} \quad 24$$

where V_t is the volume of the loop and \dot{m}_{ss} is the mass flow rate at steady state. Since a considerable amount of local unsteady flow behaviour (generation of plumes etc.) was expected, a conservative time-step was obtained by choosing to resolve a single circulation in at least 2,000 steps, increasing with the Ra_m of the case. Solutions were marched in time until the flow field either settled to a statistically steady state or to a point where it could be judged unlikely to settle to a steady state within a reasonable amount of further computation. In some cases this was up to $\mathcal{O}(10^5)$ timesteps.

3.4 CFD Model Solver

The computations reported as part of this work have been computed using an extended version of the STREAM code (Lien & Leschziner 1994a), which is a fully elliptic 3D finite volume solver capable of handling multi-block structured non-orthogonal meshes. It uses a co-located grid arrangement where all variables are stored at the cell centres and a Rhie and Chow interpolation scheme to obtain velocities at cell faces.

Convective terms for all transport equations have been treated with the Upstream Monotonic Interpolation for Scalar Transport (UMIST) scheme of (Lien & Leschziner 1994b), which is a bounded, monotonic implementation of the quadratic QUICK interpolation scheme. The second order accurate Crank-Nicolson scheme is used for time discretization. The code utilizes the standardized Message Passing Interface (MPI) for parallelisation. As a standard general 3D finite-volume solver, results obtained with the STREAM code are expected to be comparable to any other CFD solver which implements and solves the equations described in Section 3.2.

4 Results

4.1 Mesh sensitivity

Mesh sensitivity tests were conducted to assess the influence of the mesh sizing on the predicted flow results for one of the cases considered, the square loop at $Ra_m = 8 \times 10^{13}$ (ncl-ra1e13-s). A higher Ra_m case was chosen since, as the Ra_m increases, the influence of the dissipative mechanisms within the flow would be expected to decrease⁵. This increases the likelihood that buoyant instabilities will grow within the flow, leading to the potential for a wider variety of unstable flow behaviour and thus stronger sensitivity to the mesh sizing.

Three meshes were considered, as detailed in Table 5, with each one providing double the node resolution around the loop of the previous. The finest mesh considered had a total node count of $N = 268,800$. The wall-normal resolution is increased slightly only for the final mesh considered, and the distance to the first near-wall node was kept constant across all meshes, since this is driven primarily by the requirement to ensure that $y^+ \approx 1$. During the time-period considered here, the maximum y^+ measured across all three cases was $y^+ = 1.8$, present only during brief periods that tend to coincide with the maximum mass flow rate. Thus the near-wall mesh resolution is considered sufficient for the turbulence modelling approach adopted and sensitivity only to the interior nodal resolution is considered here. The time-step for all three cases is kept the same.

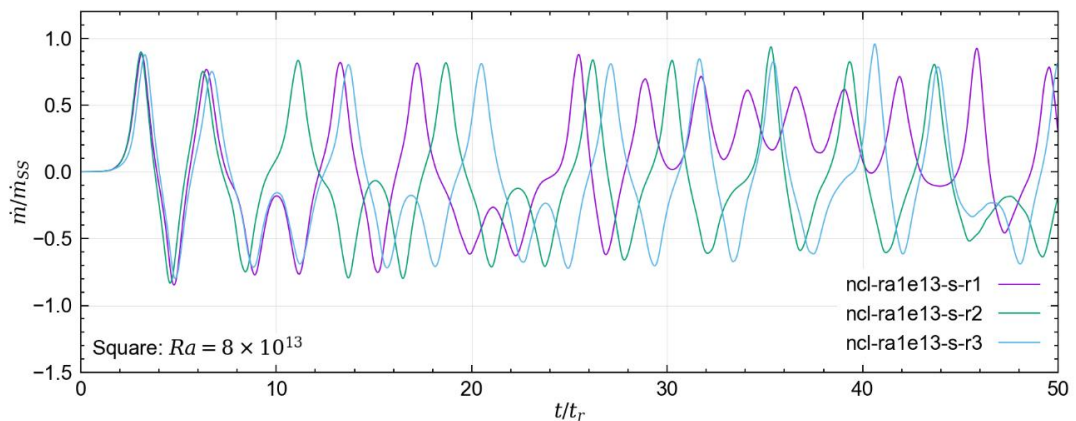


Figure 7: Time-history plots of normalized mass flow rate for the square loop at $Ra_m = 8 \times 10^{13}$. Negative mass flow rate implies a change of flow direction. Three meshes of increasing node resolution are considered for an initial period up to $t/t_r = 50$, see Table 5 for details.

Time-history plots of the mass flow rate within the loop for the three of the meshes considered are presented in Figure 9. Detailed discussion on the predicted behaviour of the system is presented later in Section 4.2, but it can be seen that the normalized mass flow rate illustrates consistent oscillatory behaviour about the zero point. Over the first 8 non-dimensional time-periods (t/t_r) the three meshes predict nearly identical behaviour. Shortly after this point, the flow captured with the intermediate resolution mesh (ncl-ra1e13-r2) undergoes a full reversal whilst the other two meshes considered only predict a “half” or “false” reversal, where the flow

⁵ Physically, the Rayleigh number quantifies the ratio between the buoyant “driving force” to the dissipative mechanisms which oppose that force, those being the diffusion of momentum and heat. Since dissipative mechanisms tend to damp flow instabilities, a higher Rayleigh number implies a greater potential for more unstable flow patterns to develop.

initially appears to be reversing (i.e. it decelerates) before accelerating back in its original direction. The mass flow rates predicted by the coarse and fine meshes stay largely in phase until around $t/t_r = 15$, when they then also deviate in a similar fashion.

Beyond $t/t_r = 15$, it is clear that initial differences in the oscillatory periods lead to large differences in phase between the mass flow rate predicted by the three meshes. However, both the amplitudes of the oscillations, and the overall flow patterns, are statistically similar. A slight exception to this can be observed with the coarsest mesh in the period $30 < t/t_r < 45$, where an extended period of oscillatory flow, without complete flow reversals, can be seen.

The temporal sensitivity to the mesh sizing is not particularly surprising in a case which exhibits highly transient and unstable flow behaviour. Even for two identical cases, very small, but persistent, differences in the flow (perhaps even due to machine number rounding) may eventually lead to time-histories which diverge from each other. Thus, it is not possible to offer definitive conclusions on which mesh would be more appropriate, beyond the notion that more nodes would generally be expected to provide a solution which better represents the true solution of the governing equations. A full statistical analysis, over a much longer time-period and over a wider range of input parameters would be required to offer any further insight.

4.2 Description of predicted start-up flow behaviour

Results of all the NCL cases conducted as part of this work (see Table 3) revealed that the flow in the loops exhibits significant start-up transients and these lead, in some cases, to oscillatory behaviour and flow reversals. In order to provide an illustrative description of this start-up behaviour, which was present in most cases considered, time-history plots at a number of monitoring points have been presented in Figure 8 for both the square and tall loop at $Ra = 8 \times 10^9$. Several snapshots of the square case from the solution time-history are also shown in Figure 9.

To normalise the flow quantities in these plots, the correlation discussed in Section 2 (Equation 6) is first used to obtain a steady-state Reynolds number, Re_{SS} , for the equivalent Gr_m/N_G combination considered. The mass flow rate is then normalised using \dot{m}_{SS} , the mass flow rate computed from the definition of Re_{SS} , Equation 7. Thus a \dot{m}/\dot{m}_{SS} of 1 in Figure 8 indicates the mass flow rate in the loop is equivalent to that predicted by the correlations. The temperature is normalised with the steady-state temperature rise across the heater, $(\Delta T_h)_{SS}$, obtained from Equation 2 using the same value of \dot{m}_{SS} .

Whilst, due to the previously mentioned lack of experimental data, validation of the results cannot be provided, the normalisation employed allows order-of-magnitude quantitative comparisons to be made against the correlations and qualitative assessments are made against physical intuitive and expected physical behaviour. Both these cases returned laminar flow in agreement with the correlation. This is discussed in more detail later in Section 4.5.

For the square loop, plots of the normalised mass flow rate in Figure 8(a) indicate that the flow initially travels clockwise around the loop before arresting and then reversing direction. The magnitude of the mass flow rate then oscillates, though it does not reverse direction, before the flow finally reverses again to travel in the clockwise direction, which is the expected direction for this loop configuration⁶. The temperature monitors in Figure 8(b) show that the bulk temperature in the loop is rising over time. This indicates that, for the time frame shown, the heat flux provided by the heater is initially dominant.

⁶ Whilst the centrally located horizontal heater does not provide a preferential direction, the vertically oriented cooler does.

Results obtained with the tall loop, presented in Figure 8(c) and Figure 8(d), show remarkably similar behaviour with flow reversals predicted at similar times but with noticeably larger peak mass flow rates. Physically this is expected, since the taller vertical sections mean the integral buoyancy force can act to impart momentum to the fluid over a much longer distance. That the overall flow pattern is the same between the two loop sizes, however, indicates that, for this Ra_m at least, $\mathcal{O}(1)$ changes to the loop height only appear to alter the response of the system to an initial transient in a quantitative, rather than qualitative, fashion. The effect of larger, order-of-magnitude changes to the input parameters on the system response is further discussed in Section 4.4 whilst the behaviour of the flow after the time-period considered here is presented in Section 4.3.

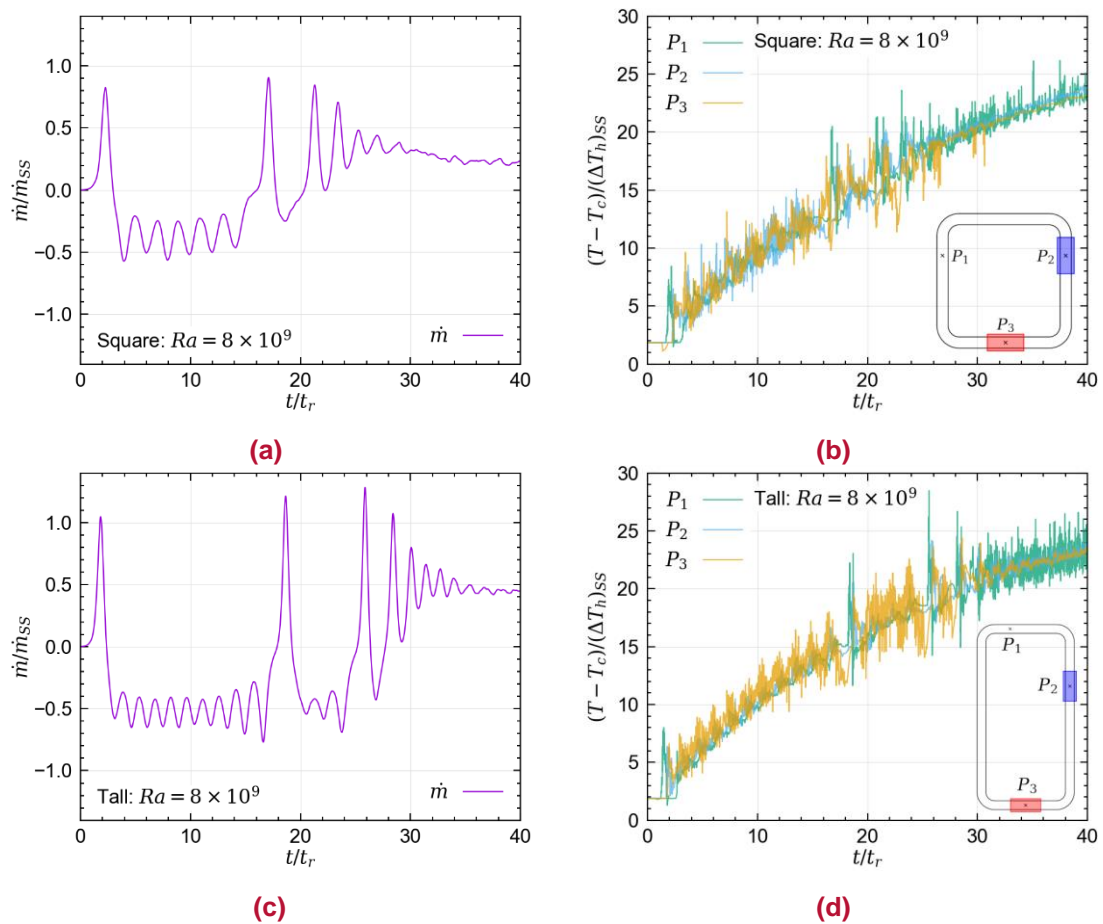


Figure 8: Initial time-history plots showing non-dimensional mass flow rate (left) and non-dimensional temperature (right), for the square (top) and tall (bottom) loop geometries at $Ra_m = 8 \times 10^9$. Monitor positions for the temperature plots are indicated inset and T_c is the temperature of the cold wall in the cooler. A positive mass flow rate indicates clockwise flow.

To elucidate the intriguing behaviour discussed above, Figure 9 presents a series of instantaneous snapshots of normalised temperature for the square loop at $Ra = 8 \times 10^9$. Initially, shown in Figure 9(a), the heat flux imparted to the fluid in the heater leads to the production of a number of buoyant plumes. These rise within the heater section of the pipe and impinge on the upper heater surface, where they travel left and right in almost equal measure. Since the monitor plots indicate that the initial heat flux provided by the heater is significantly higher than the outgoing heat flux within the cooler, the cooler does not cool the fluid enough to produce an equivalent effect in the right vertical leg. The hot fluid can then be seen to rise up

the left hand leg in Figure 9(b) where, since the left leg is now on average less dense than the right leg, clockwise circulation of the fluid is initiated. The inertia imparted to the fluid by this circulation then takes the hot fluid “plug” around the top leg and into the right leg, drawing cooler fluid from the right leg through the heater. Since, in this case, the fluid passes through the heater too quickly for it to significantly reduce in density, the denser (heavier) fluid in the left leg (as shown in Figure 9(c)) causes the flow to reverse direction and circulation commences in the anti-clockwise direction.

The above description forms the basic physical mechanism for reversals and oscillatory behaviour; any imbalance between the average densities of the fluid in the left and right leg will lead to a resultant buoyant force, either slowing or accelerating the fluid. Changes in the density (temperature) imbalance, and thus the resultant flow rate, are affected by the two dissipation mechanisms (viscous and thermal) and the two external sources of heat transfer (cooler and heater), which will themselves impose different thermal time scales owing to differences in the thermal boundary conditions. If any of these effects are out of phase, then overshooting may occur and instabilities may grow. In the case considered here, this manifests in the form of oscillatory flow behaviour and flow reversals.

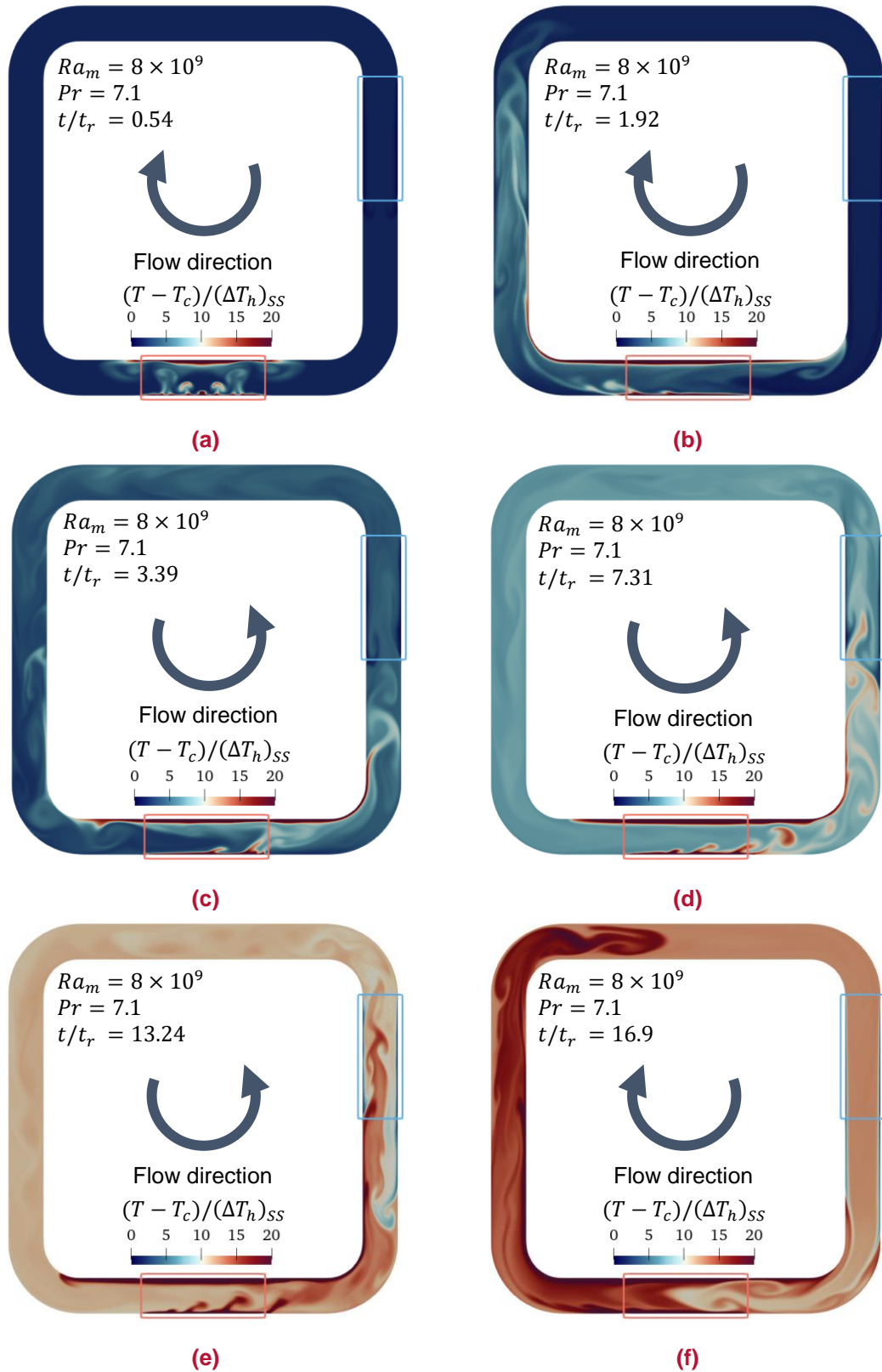
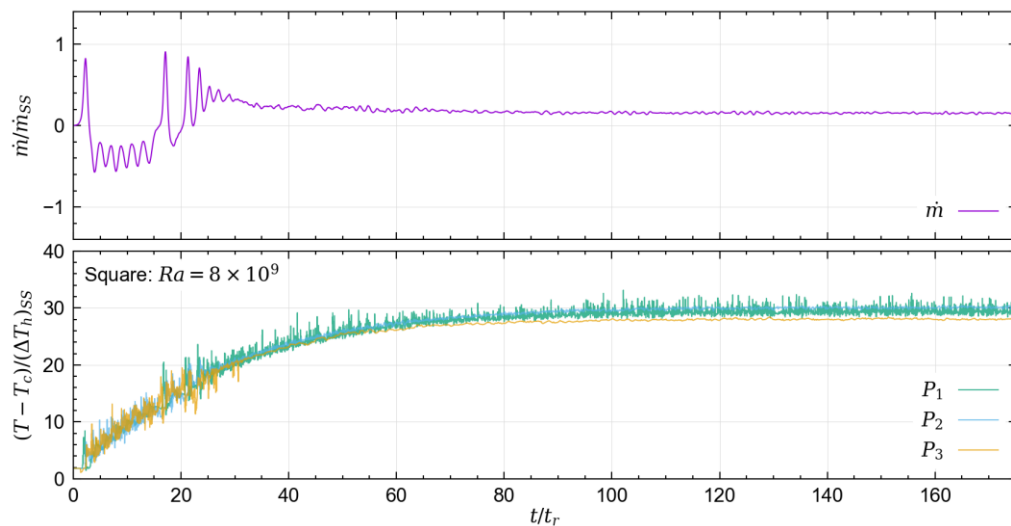


Figure 9: Instantaneous contours of normalised temperature at selected non-dimensional time values for the square loop at $Ra = 8 \times 10^9$

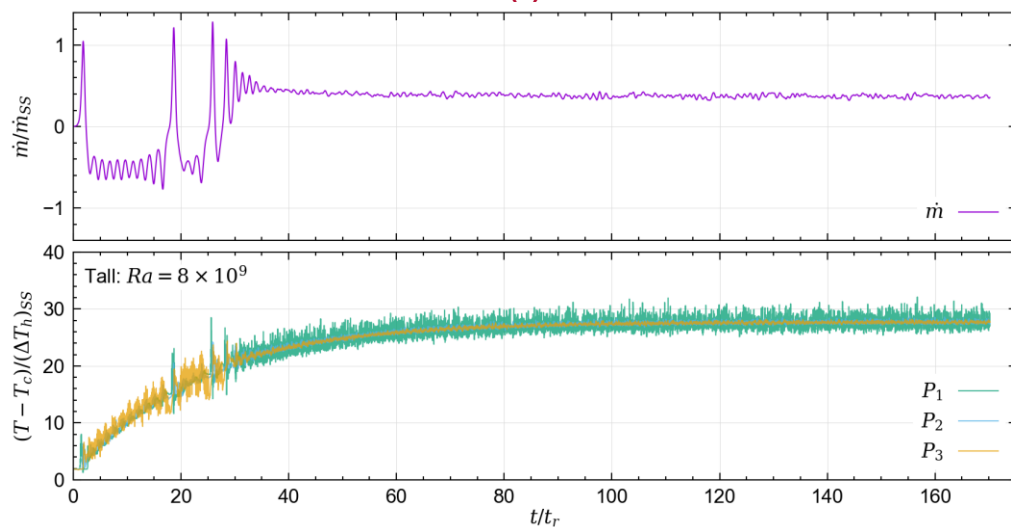
4.3 Statistically steady-state behaviour

Whilst the results of the square and tall loop cases at $Ra_m = 8 \times 10^9$ discussed in Section 4.2 did reveal significant initial flow transients, the mass flow plots presented in Figure 8 do suggest the flow does appear to begin to settle towards the end of the time-period considered. Further advancing the computation of these cases in time confirms this suggestion, as can be seen from the full time-history presented in Figure 10.

For both loop geometries, normalised mass flow rate monitors appear to settle after approximately $t/t_r = 40$. Whilst the flow is still clearly transient, as evidenced by the remaining variations in both the mass flow rate and temperature monitors, this indicates the flow dynamics have shifted towards a more stable pattern. The continuously decreasing gradient shown by the normalized temperature monitors indicates that this occurs as the loop approaches thermal equilibrium, since the bulk temperature in the loop is no longer changing statistically in time (i.e. when averaged over a number of t_r periods).



(a)



(b)

Figure 10: Normalised mass flow rate and temperature monitors for (a) the square loop and (b) the tall loop at $Ra_m = 8 \times 10^9$. Monitor locations are as indicated in Figure 8.

Time-averages of the flow were taken from approximately $t/t_r = 50$ until the end of the time-period shown in Figure 10 ($t/t_r \approx 175$). The resulting time-averaged contours of normalised velocity and temperature are presented for both square and tall cases in Figure 11 and Figure 12 respectively. The results for the square loop reveal an interesting flow feature in the lower right elbow which is present on-average. Warmer fluid from the heater leaks around the upper surface of the lower right elbow leading to impingement against the cooler fluid sinking down the right leg from the cooler. This diversion causes the flow profile to meander slightly as it navigates the lower right corner before straightening up after it passes through the heater. The results for the tall loop, shown in Figure 12 do not reveal such a feature.

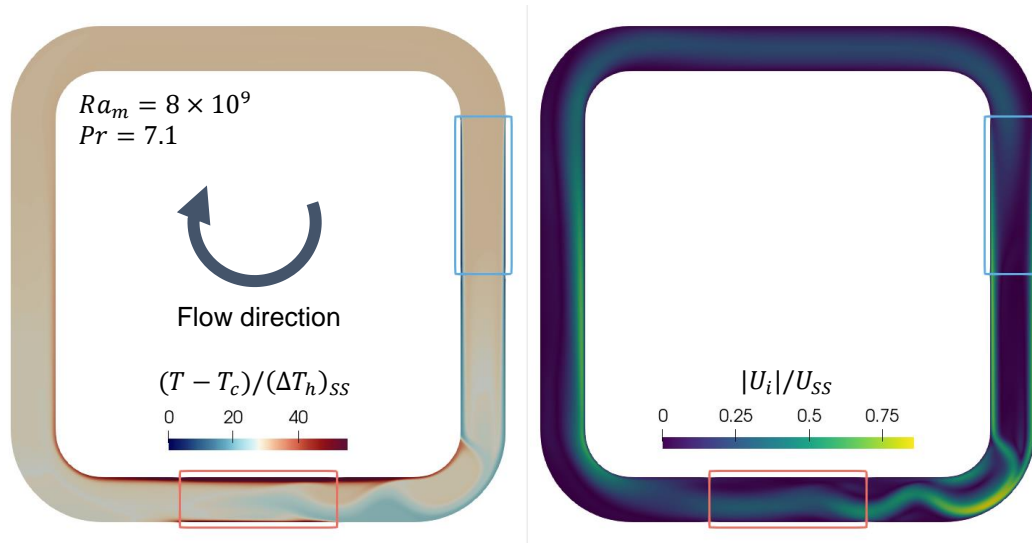


Figure 11: Contours of long-term time averaged non-dimensional temperature (left) and velocity (right) for the square loop at $Ra = 8 \times 10^9$. U_{SS} is a velocity scale formed from \dot{m}_{SS} .

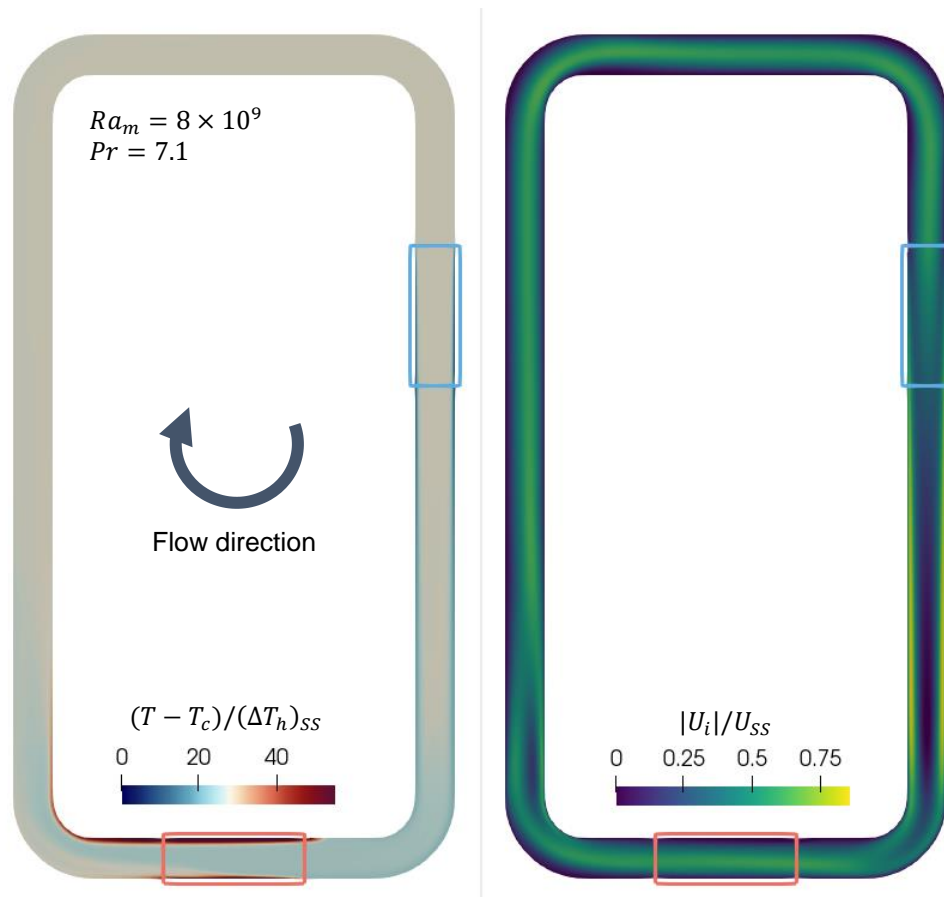


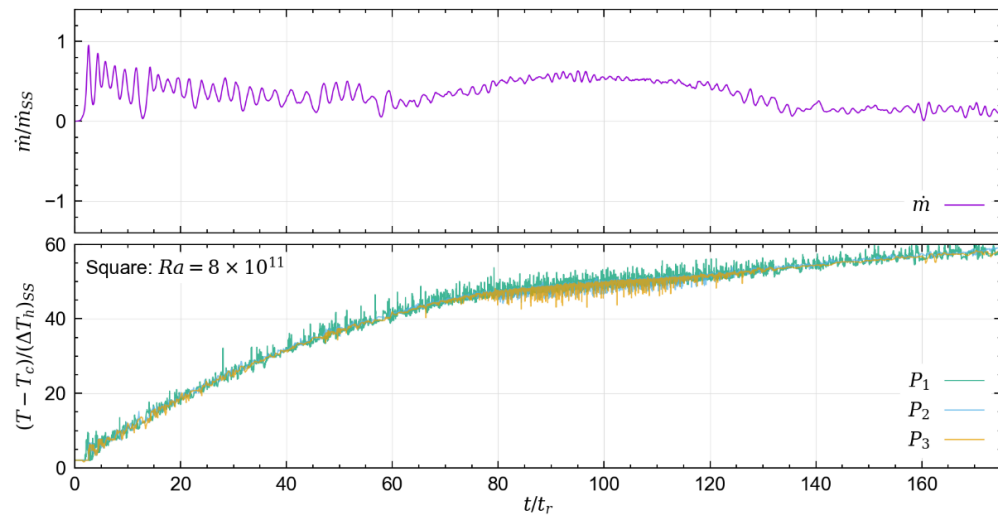
Figure 12: Contours of long-term time averaged non-dimensional temperature (left) and velocity (right) for the tall case at $Ra = 8 \times 10^9$. U_{SS} is a velocity scale formed from \dot{m}_{SS} .

4.4 Predicted effect of increasing Rayleigh number

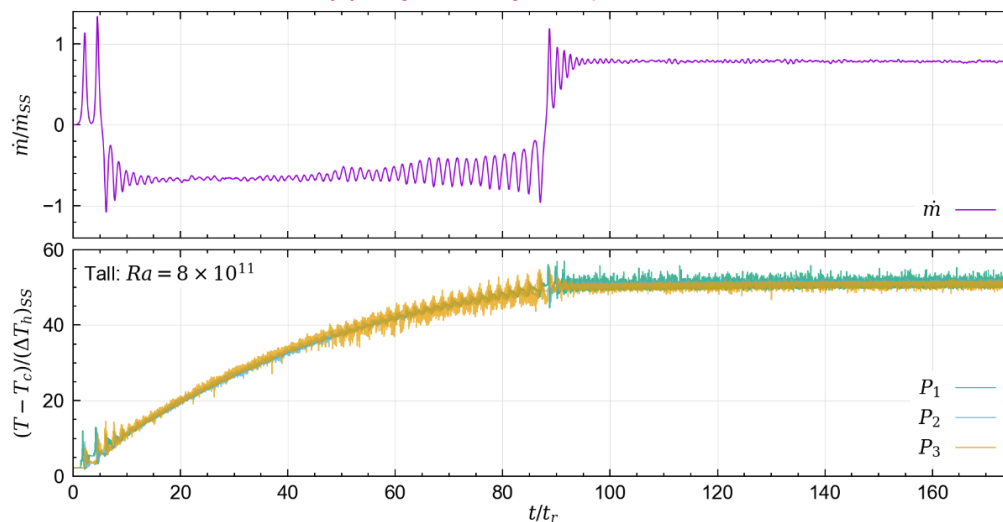
Physically, the Rayleigh number quantifies the ratio between the buoyant “driving force” and the dissipative mechanisms which oppose that force; the diffusion of momentum and heat. Since dissipative mechanisms tend to damp flow instabilities, a higher Rayleigh number would be expected to enable more unstable flow patterns to develop. Results at the higher $Ra_m = 8 \times 10^{13}$ were briefly seen in Section 4.1 when discussing the sensitivity of the results to the mesh sizing. Those, and further results obtained with both loops at $Ra_m = 8 \times 10^{11}$ and the square loop at $Ra_m = 8 \times 10^{15}$ are considered in more detail below.

Time-history plots of normalised mass flow rate and temperature for both loops at $Ra_m = 8 \times 10^{11}$ are presented in Figure 13. The flow patterns exhibited by the square loop indicate less coherent behaviour than that seen at $Ra_m = 8 \times 10^9$ (Figure 10), with no flow reversals and indeterminate oscillations. This is despite temperature monitors initially showing largely similar thermal changes between cases. In contrast, the tall loop (Figure 13b) exhibits behaviour qualitatively similar to that seen at $Ra_m = 8 \times 10^9$; an initial flow reversal following by a periodic of relatively regular oscillatory behaviour, before reverting back to the original direction and settling into an apparently statistically steady-state. The period of counter-clockwise flow (i.e. a negative mass flow rate in Figure 13b), however, persists for a longer period of time.

Oscillations in the mass flow rate initially appear to decay and remain relatively small until $t/t_r = 40$, where they then begin to grow, culminating in the final flow reversal at $t/t_r = 90$.



(a) Square loop; $Ra_m = 8 \times 10^{11}$



(b) Tall loop; $Ra = 8 \times 10^{11}$

Figure 13: Normalised mass flow rate and temperature monitors for (a) the square loop and (b) the tall loop at $Ra_m = 8 \times 10^9$. Monitor locations are as indicated in Figure 8.

The change in loop geometry was only seen to result in quantitative differences at the lower Ra_m , whereas significant qualitative differences are seen at $Ra_m = 8 \times 10^{11}$. Though a two order-of-magnitude increase in Ra_m has clearly resulted in significant changes to the flow dynamics of the NCL system, the increase in loop length actually results in a reduction in the Gr_m/N_G parameter, since N_G increases and Gr_m remains fixed (as both Ra_m and Pr are kept constant across both geometries). Thus if the behaviour of the system at $Ra_m = 8 \times 10^{13}$ is more unstable, as Figure 13 suggests it is, then the more modest $\mathcal{O}(1)$ reduction in Gr_m/N_G offered by the taller loop might be enough to result in behaviour more similar to that seen at $Ra_m = 8 \times 10^{11}$.

As Ra_m is increased further, to $Ra_m = 8 \times 10^{13}$, another significant change in qualitative flow behaviour is seen as illustrated by the time-history plots for both loop geometries presented in

Figure 14. Continual flow reversals are seen, interspersed with occasional “half” reversals, where the flow initially slows towards zero before accelerating again without changing direction. Unlike at lower Ra_m , the amplitude of the oscillations remains of the same order as \dot{m}_{SS} , and do not appear to change significantly across the entire time-history. This is again despite temperature monitors implying a similar thermal response to lower Ra_m . Comparisons between the loop geometries at this Ra_m indicate quantitative differences in both the amplitude (though they are of the same order) and frequency of the oscillations. Further computation would be required to determine the stability of this flow pattern.

A further and final increase in Ra_m to 8×10^{15} is considered only for the square loop in Figure 15. There are again some qualitative differences in the predicted flow patterns, with a noticeable reduction in the number of total flow reversals over that seen at $Ra_m = 8 \times 10^{13}$ and an increased tendency for the flow to travel counter-clockwise. Contrary to the cases at lower Ra_m , however, the temperature monitors indicate higher, and continually increasing, bulk temperatures within the loop over the time-period considered.

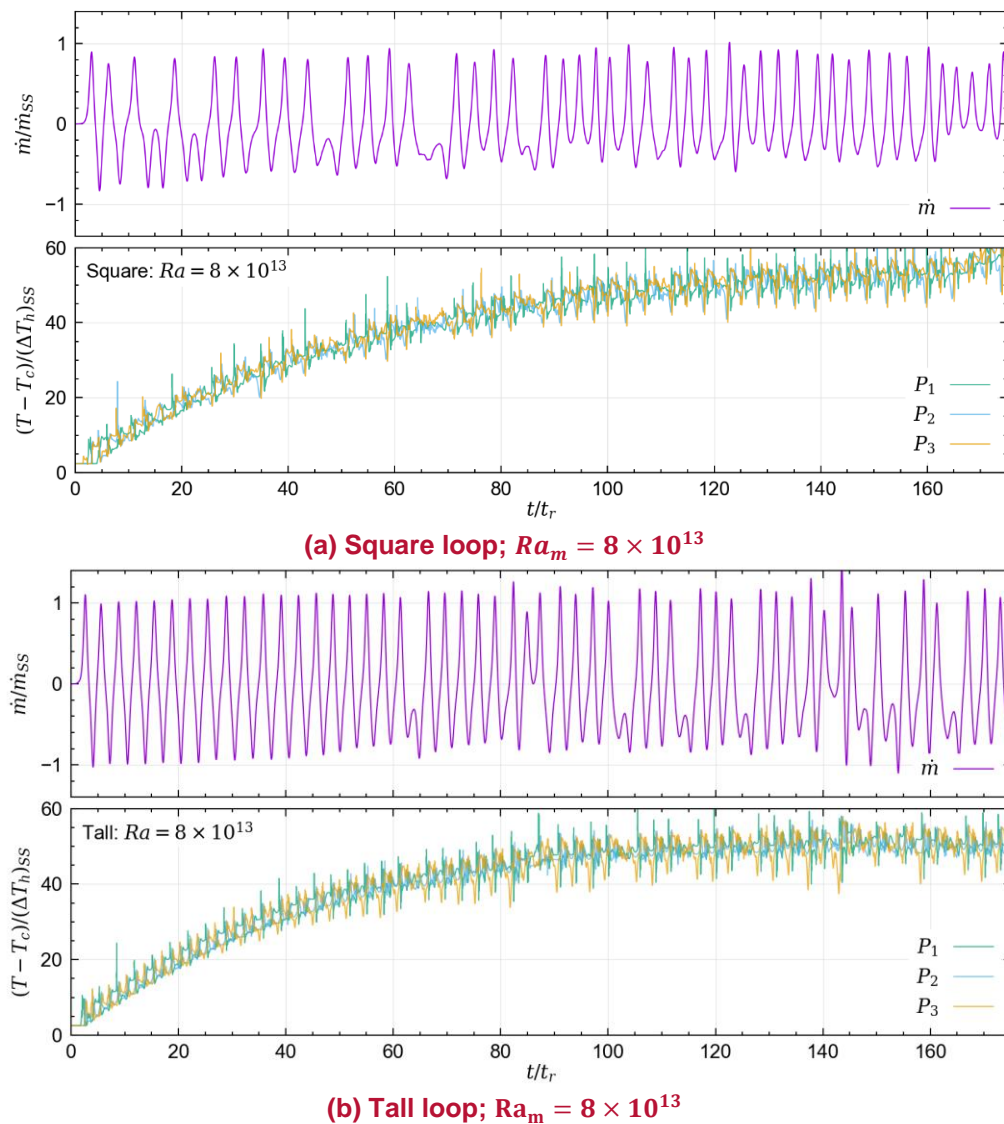


Figure 14: Normalised mass flow rate and temperature monitors for (a) the square loop and (b) the tall loop at $Ra_m = 8 \times 10^9$. Monitor locations are as indicated in Figure 8.

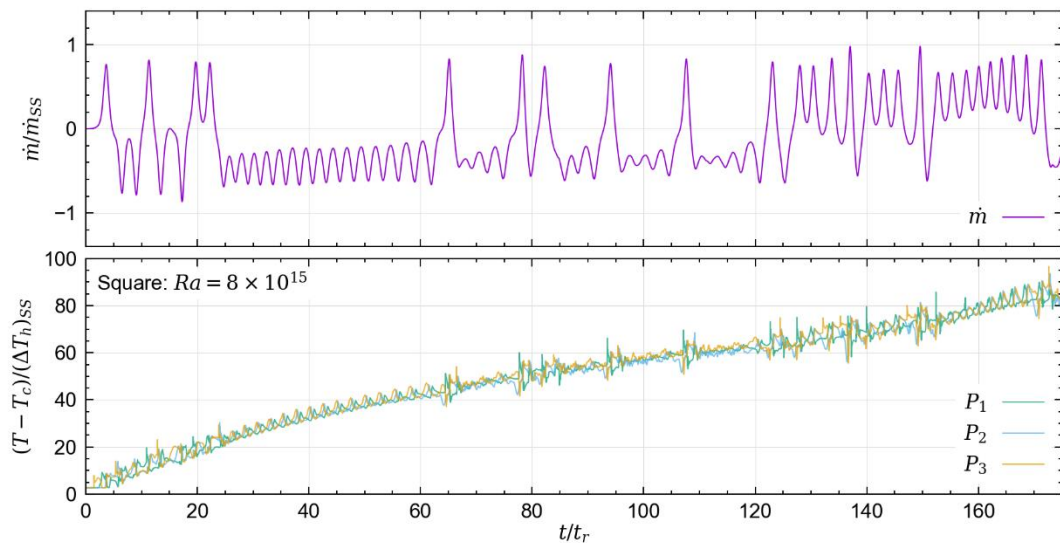


Figure 15: Normalised mass flow rate and temperature monitors for the square loop at $Ra_m = 8 \times 10^{15}$. Monitor locations are as indicated in Figure 8.

4.5 Comparisons with existing correlations

In order to provide some limited quantitative assessment of the flow predictions, Figure 16 reproduces the $Re_{SS} - Gr_m/N_G$ parameter map presented in Figure 3 and adds the predictions of Reynolds number (against Gr_m/N_G) for the three cases identified in the previous sections which had demonstrated statistically steady behaviour: the square and tall loop at $Ra_m = 8 \times 10^9$ and the tall loop at $Ra_m = 8 \times 10^{11}$.

Excellent agreement can be seen for the tall loop at $Ra_m = 8 \times 10^{11}$. Whilst all three simulations plotted tended to predict lower Re_{SS} than the correlations suggest, the comparisons do indicate that the correct trend is being reproduced as the Gr_m/N_G parameter combination increases. Additionally, variations in the normalised mass flow rate for all cases considered in previous sections are typically $\mathcal{O}(1)$, indicating broad order-of-magnitude agreement with the correlations.

The discrepancy between the Re_{SS} predicted by the square loop at $Ra_m = 8 \times 10^9$ and the correlations is, however, particularly noticeable since, unlike the tall loop at the same Ra_m , the predicted Re_{SS} is also outside of the range of the experimental data plotted in Figure 16. Since the reported flow is laminar (in agreement with the correlations) the differences cannot be attributed to any deficiencies in the approach to modelling the turbulence. The differences are potentially due to the two-dimensional planar nature of the cases considered, since all experimental data plotted in Figure 16 represent three-dimensional loops with pipe type geometry, but this is not consistent across all three simulations plotted.

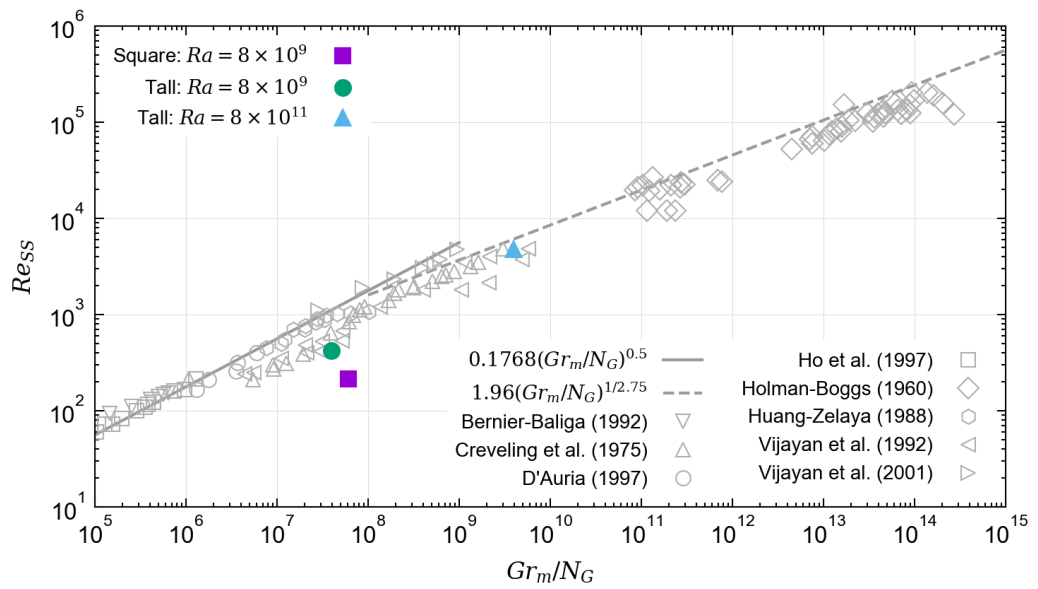


Figure 16: Comparison of resultant Reynolds number for three cases considered in this study which demonstrated statistically steady-state behaviour with correlations of Vijayan (2002) defined as per Table 1 and Equation 6.

5 Conclusions

This report presents CFD simulations of a single-phase natural circulation loop with the aim of providing insight into the complex transient natural convection phenomena predicted to occur. The loops have relevance to passive cooling systems which are increasingly being utilized by future next generation reactor designs. A series of two-dimensional simulations have been performed, covering a wide parameter range ($8 \times 10^9 < Ra_m < 8 \times 10^{15}$) and two loop designs of differing aspect ratio. Modelling the loops as two-dimensional significantly reduces the time required for computations whilst still capturing a significant proportion of the flow physics.

The results indicate that the CFD methodology predicts initial thermal transients that lead to the establishment of significant oscillatory flow behaviour. Differences between the timescale associated with the thermal field and the timescale associated with the flow geometry lead to the prediction of flow reversals which, in some cases, continue to occur in an oscillatory fashion. Examination of the mass flow rate and temperature time-history for each case reveal that changes to the imposed Ra_m can lead to considerable differences in predicted flow behaviour:

- ▶ At $Ra_m = 8 \times 10^9$, flow predictions in both loop geometries displayed the same qualitative behaviour; initially oscillatory with complete reversals but later transitioned and settled into a statistically steady-state.
- ▶ At $Ra_m = 8 \times 10^{11}$ greater differences are predicted; the tall geometry eventually settled into a statistically steady-state after flowing in a direction opposite to expectations for around half of the complete time-history considered, whilst the flow in the square loop presented much more irregular behaviour.
- ▶ At $Ra_m = 8 \times 10^{13}$ continuous flow reversals are predicted, despite temperature monitors indicating that the system was approaching thermal equilibrium.

Comparisons with existing experimental works and established correlations were favourable and predicted the correct trend, despite the two-dimensional nature of the CFD computations. Overall, a number of key conclusions can be drawn from this work:

- ▶ A two-dimensional loop model, with a linear eddy-viscosity turbulence model, is able to broadly reproduce the correct statistical system response as Ra_m is increased.
- ▶ The Unsteady Reynolds-averaged Navier-Stokes framework is capable of reproducing complex transient buoyant features which are, at least with the model considered in this work, integral to the dynamic evolution of the flow within the loop.
- ▶ Order-of-magnitude increases in Ra_m are seen to significantly alter the predicted dynamic response of the system. If validated, this has implications for real loops whose power inputs might additionally vary with time.
- ▶ Complete mesh independence is unlikely to be fully achieved, owing to the highly unstable, almost chaotic, transient nature of the problem. A detailed mesh sensitivity study should always be conducted with the aim to ascertain the extent to which the mesh resolution alters the flow statistics, rather than attempting to accurately reproduce all of the unsteady motions associated with any transients.

Whilst the two-dimensional model allows solutions to be obtained relatively quickly, and has allowed a number of different input parameters and geometries to be assessed in this work, future research should aim to assess the influence of the following modelling elements:

- ▶ The use of the Boussinesq approximation for buoyancy. Results should be compared against a case computed with fully variable, temperature-dependent, properties.

- ▶ The restriction of the flow geometry to two-dimensions. Full three-dimensional results, though considerably more expensive, should be obtained and compared.
- ▶ Simplified loop geometry. Real passive cooling loops in reactors are much more geometrically complex; they are likely to have a much larger H/D_h ratio and include more geometric features (bends, valves etc.) than the loops considered here. Whilst additional losses imposed by these geometric features may improve system stability, they may also introduce additional flow structures (secondary flows, for instance) which may interact with existing structures in ways that are likely to be difficult to pre-empt.
- ▶ The positioning of the heater and cooler. Alternative arrangements of the heater and cooler will likely have a significant impact on the stability of the system. In the loop considered in this work, placing the heater on the left vertical leg should improve stability.
- ▶ The influence of both initial and boundary conditions. Loops considered here started from a scenario in which the heat flux from the heater was initially dominant. The influence of conjugate heat transfer should also be considered.

6 References

- Ammour, D., Craft, T., & Iacovides, H. (2013). Highly Resolved LES and URANS of Turbulent Buoyancy-Driven Flow Within Inclined Differentially-Heated Enclosures. *Flow, Turbulence and Combustion*, **91**(3), 669–696.
- Basu, D. N., Bhattacharyya, S., & Das, P. K. (2014). A review of modern advances in analyses and applications of single-phase natural circulation loop in nuclear thermal hydraulics. *Nuclear Engineering and Design*, **280**, 326–348.
- Craft, T. J., Gerasimov, A. V., Iacovides, H., Kidger, J. W., & Launder, B. E. (2004). The negatively buoyant turbulent wall jet: performance of alternative options in RANS modelling. *International Journal of Heat and Fluid Flow*, **25**(5), 809–823.
- Gen IV International Forum. (2013). *Technology Roadmap Update for Generation IV Nuclear Energy Systems*.
- IAEA. (2005). *Natural Circulation in Water Cooled Nuclear Power Plants* (No. IAEA-TECDOC-1474). Retrieved from <http://www-pub.iaea.org/books/IAEABooks/7376/Natural-Circulation-in-Water-Cooled-Nuclear-Power-Plants>
- IAEA. (2009). *Passive safety systems and natural circulation in water cooled nuclear power plants*. (Technical Document No. IAEA-TECDOC-1624), Vienna, Austria: International Atomic Energy Agency. Retrieved from <https://www-pub.iaea.org/books/iaeabooks/8192/Passive-Safety-Systems-and-Natural-Circulation-in-Water-Cooled-Nuclear-Power-Plants>
- Kudariyawar, J. Y., Vaidya, A. M., Maheshwari, N. K., & Satyamurthy, P. (2016). Computational study of instabilities in a rectangular natural circulation loop using 3D CFD simulation. *International Journal of Thermal Sciences*, **101**, 193–206.
- Launder, B., & Sharma, B. (1974). Application of the energy-dissipation model of turbulence to the calculation of flow near a spinning disc. *Letters in Heat and Mass Transfer*, **1**(2), 131–137.
- Lien, F., & Leschziner, M. (1994a). A general non-orthogonal collocated finite volume algorithm for turbulent flow at all speeds incorporating second-moment turbulence-transport closure, Part 1: Computational implementation. *Computer Methods in Applied Mechanics and Engineering*, **114**(1–2), 123–148.
- Lien, F., & Leschziner, M. (1994b). Upstream monotonic interpolation for scalar transport with application to complex turbulent flows. *International Journal for Numerical Methods in Fluids*, **19**(6), 527–548.
- Misale, M., Garibaldi, P., Passos, J. C., & de Bitencourt, G. G. (2007). Experiments in a single-phase natural circulation mini-loop. *Experimental Thermal and Fluid Science*, **31**(8), 1111–1120.
- Omranian, A., Craft, T. J., & Iacovides, H. (2014). The computation of buoyant flows in differentially heated inclined cavities. *International Journal of Heat and Mass Transfer*, **77**, 1–16.
- Schulz, T. L. (2006). Westinghouse AP1000 advanced passive plant. *Nuclear Engineering and Design*, **236**(14), 1547–1557.
- Vijayan, P. K. (2002). Experimental observations on the general trends of the steady state and stability behaviour of single-phase natural circulation loops. *Nuclear Engineering and Design*, **215**(1), 139–152.
- Vijayan, P. K., & Austregesilo, H. (1994). Scaling laws for single-phase natural circulation loops. *Nuclear Engineering and Design*, **152**(1–3), 331–347.

Vijayan, P. K., Mehta., S. K., & Date, A. W. (1991). On the steady-state performance of natural circulation loops. *International Journal of Heat and Mass Transfer*, **34**(9), 2219–2230.

Wang, J. Y., Chuang, T. J., & Ferng, Y. M. (2013). CFD investigating flow and heat transfer characteristics in a natural circulation loop. *Annals of Nuclear Energy*, **58**, 65–71.

Wilson, D. R., Craft, T. J., & Iacovides, H. (2015). Application of Reynolds stress transport turbulence closure models to flows affected by Lorentz and buoyancy forces. *International Journal of Heat and Fluid Flow*, **55**, 180–197.

Wilson, D. R. (2019). *Project FORTE - Nuclear Thermal Hydraulics Research and Development - Assessment of RANS turbulence model performance in tight lattice LWR fuel sub-channels*. Frazer-Nash Consultancy, FNC 53798/48654R, Issue 1.

DOCUMENT INFORMATION

Project : Project FORTE - Nuclear Thermal Hydraulics Research & Development
Report Title : Application of CFD to single-phase Natural Convection Loops for Nuclear Passive Safety Systems
Client : Department for Business, Energy and Industrial Strategy (BEIS)

Report No. : FNC 53798/48655R	Compiled By : Dr D. Wilson (The University of Manchester)
Issue No. : 1	Verified By : Prof H. Iacovides (The University of Manchester)
Date : August 2019	Approved By : R. Underhill

Legal Statement

This document has been prepared for the UK Government Department for Business, Energy and Industrial Strategy (BEIS) by Frazer-Nash Consultancy Ltd, and any statements contained herein referring to 'we' or 'our' shall apply to Frazer-Nash Consultancy and BEIS both individually and jointly.

The Copyright in this work is vested in Frazer-Nash Consultancy Limited. Reproduction in whole or in part or use for tendering or manufacturing purposes is prohibited except under an agreement with or with the written consent of Frazer-Nash Consultancy Limited and then only on the condition that this notice is included in any such reproduction.

This document is provided for general information only. It is not intended to amount to advice or suggestions on which any party should, or can, rely. You must obtain professional or specialist advice before taking or refraining from taking any action on the basis of the content of this document.

We make no representations and give no warranties or guarantees, whether express or implied, that the content of this document is accurate, complete, up to date, free from any third party encumbrances or fit for any particular purpose. We disclaim to the maximum extent permissible and accept no responsibility for the consequences of this document being relied upon by you, any other party or parties, or being used for any purpose, or containing any error or omission.

Except for death or personal injury caused by our negligence or any other liability which may not be excluded by an applicable law, we will not be liable to any party placing any form of reliance on the document for any loss or damage, whether in contract, tort (including negligence) breach of statutory duty, or otherwise, even if foreseeable, arising under or in connection with use of or reliance on any content of this document in whole or in part.

This document represents the views of Frazer-Nash Consultancy Limited and does not represent the views of BEIS or the UK Government more widely.

Originating Office: FRAZER-NASH CONSULTANCY LIMITED
The Cube, 1 Lower Lamb Street, Bristol, BS1 5UD
T: +44 (0)117 9226242 F: +44 (0)117 9468924 W: www.fnc.co.uk



Frazer-Nash Consultancy Ltd

The Cube
1 Lower Lamb Street
Bristol
BS1 5UD

T +44 (0)117 9226242
F +44 (0)117 9468924

www.fnc.co.uk

Offices at:
Bristol, Burton-on-Trent, Dorchester,
Dorking, Glasgow, Plymouth, Warrington
and Adelaide